Coseismic surface deformation from air photos: The Kickapoo step over in the 1992 Landers rupture

Rémi Michel[1] and Jean-Philippe Avouac[2]

Received 11 April 2005; revised 13 September 2005; accepted 16 November 2005; published 21 March 2006.

[1] Coseismic deformation of the ground can be measured from aerial views taken before and after an earthquake. We chose the area of the Kickapoo-Landers step over along the 1992 Landers earthquake zone, using air photos (scale 1:40,000) scanned at 0.4 m resolution. Two photos acquired after the earthquake are used to assess the accuracy and to evaluate various sources of noise. Optical distortions, film deformation, scanning errors, or errors in viewing parameters can yield metric bias at wavelength larger than 1 km. Offset field at shorter wavelength is more reliable and mainly affected by temporal decorrelation of the images induced by changes in radiometry with time. Temporal decorrelation and resulting uncertainty on offsets are estimated locally from the correlation degree between the images. Relative surface displacements are measured independently every about 15 m and with uncertainty typically below 10 cm (RMS). The offset field reveals most of the surface ruptures mapped in the field. The fault slip is accurate to about 7 cm (RMS) and measured independently every 200 m from stacked profiles. Slip distribution compares well with field measurements at the kilometric scale but reveals local discrepancies suggesting that deformation is generally, although not systematically, localized on the major fault zone located in the field. This type of data can provide useful insight into the fault zone's mechanical properties. Our measurements indicate that elastic coseismic strain near the fault zone can be as large as 0.5×10^{-3}, while anelastic yielding was attained for strain in excess of about $1-2 \times 10^{-3}$.

Citation: Michel, R., and J.-P. Avouac (2006), Coseismic surface deformation from air photos: The Kickapoo step over in the 1992 Landers rupture, *J. Geophys. Res.*, *111*, B03408, doi:10.1029/2005JB003776.

1. Introduction

[2] Earthquake ruptures can form a sharp, knife edge, fault trace or a rather broad shear zone which can be a few kilometers wide. The geometry of surface ruptures and measurement of the ground deformation are key observations to investigate earthquake mechanics and faults zone's constitutive properties [e.g., *Fialko*, 2004a]. First, the measurement of fault trace and surface slip distribution are primary sources of information on the fault geometry and coseismic slip distribution at depth. Combined with seismological observations, these data provide boundaries conditions helpful to constrain the kinematics of seismic rupture. In additions fault geometry and associated slip distribution might be a key factor determining dynamic rupture, the conditions for propagation or arrest of the seismic rupture, and the frequency content of the radiated seismic waves [e.g., *Hernandez et al.*, 1999]. Better understanding coseismic ground deformation is also of interest to seismic engineering since a significant fraction of near-fault damage to engineered structures result from permanent ground deformation rather than from ground shaking. Measuring coseismic deformation in the near field is therefore a major issue in seismotectonics. However, this piece of information is not easy to gather, so there is a need for methodological improvements.

[3] We first discuss the limitation of field investigations and the potential of remote sensing techniques. We next show that these measurements can be made from correlation of air photos taken before and after coseismic deformation. We chose a test case that has received much attention already, the Kickapoo step over along the fault trace of the 1992, M_w 7.3, Landers earthquake, making it possible to compare our measurements with detailed field observations [*Spotila and Sieh*, 1995; *Johnson et al.*, 1994; *Sowers et al.*, 1994; *Peltzer et al.*, 1994]. The primary objective of this analysis is to assess the potential and limitations of the technique and identify the main source of uncertainties. In section 8 we also point to some seismotectonics implications of our measurements.

2. Measuring Fault Zone Deformation From Field Investigations and Remote Sensing Technique

[4] Geometry of fault ruptures and coseismic slip are generally determined from investigations in the field. While surface fractures are relatively easy to detect and map, it is

[1]Laboratoire de Détection et de Géophysique, CEA, Bruyères-le-Châtel, France.
[2]Tectonics Observatory, Geological and Planetary Sciences, California Institute of Technology, Pasadena, California, USA.

0148-0227/06/2005JB003776$09.00

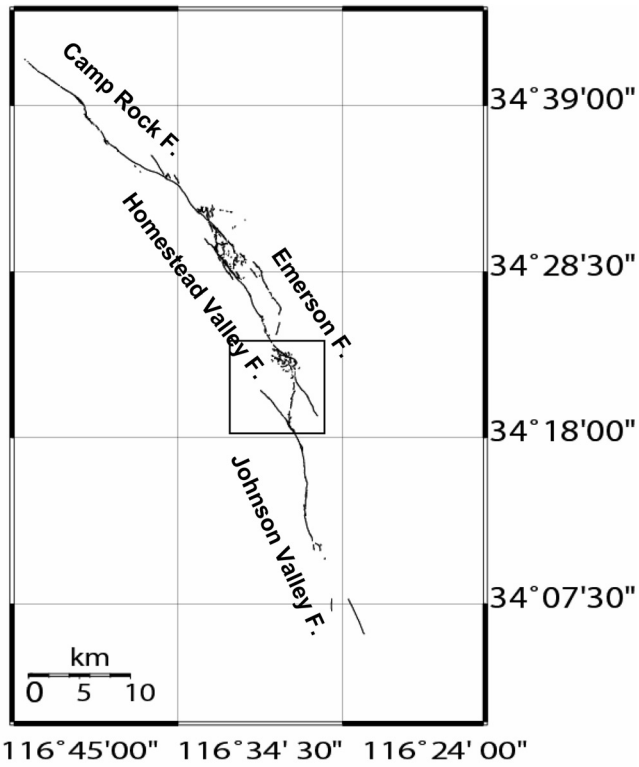

Figure 1. Map of the 1992 M_w 7.3 Landers surface ruptures after *Sieh et al.* [1993]. Box indicates the Landers-Kickapoo step over.

not always easy to accurately measure offsets across the fault zone. The measurement of offset parallel to the fault trace (including the strike-slip and vertical components) can generally be made only at a limited number of sites where natural or anthropogenic features which span the fault zone, have been offset by a measurable amount [*Yeats et al.*, 1997; *Weldon et al.*, 1996]. Even in a favorable case, the uncertainty in the geometry of feature before coseismic deformation leads to considerable uncertainty on the measurement of coseismic displacement across the fault zone. The component of displacement perpendicular to the fault is generally not directly measurable, and is generally inferred from the vertical component of fault displacement assuming some fault dip angle. In the case where ruptures have complex geometries or form broad zones of distributed faulting, estimating the total slip across the fault zone is even more difficult. In addition, the zone of coseismic anelastic strain might be significantly broader than the zone where ruptures are clearly seen at the surface [e.g., *McGill and Rubin*, 1999; *Simons et al.*, 2002; *Binet and Bollinger*, 2005]. In the case of the Landers earthquake (Figure 1), surface slip was measured in the field at a considerable number of points along the fault [e.g., *Sieh et al.*, 1993; *Sowers et al.*, 1994]. The total slip across the fault zone, estimated by adding offsets measured on the various ruptures recognized in the field, show significant variations along the rupture. Indeed it has been observed that coseismic ground shear was distributed at some places in a zone possibly as broad as 1–2 km and may amount to as much as 20% of the total slip across the fault zone [e.g., *Johnson et al.*, 1994; *McGill and Rubin*, 1999; *Yeats et al.*, 1997]. It is unclear whether this variability reflects near surface complexities of deformation or slip variability on the seismic fault at depth.

[5] Imaging ground deformation in the fault zone using remote sensing techniques should help overcome some of the limitations of field measurements. Several techniques based on satellite imagery might be used. Synthetic aperture radar (SAR) interferometry is a powerful technique to measure coseismic ground deformation [*Massonnet et al.*, 1993], but it generally fails near the field where large displacements result in poorly correlated images and eventually decorrelation of radar echoes [*Michel et al.*, 1999a; *Simons et al.*, 2002]. The use of subpixel correlation of SAR amplitude images can partially supplement this technique as it provides an unambiguous measurement of both the track-parallel and track-perpendicular components of the ground displacement [*Michel et al.*, 1999a; *Peltzer et al.*, 1999; *Simons et al.*, 2002; *Fialko*, 2004a]. The use of optical satellite imagery is an alternative technique [*Crippen*, 1992; *Van Puymbroeck et al.*, 2000; *Dominguez et al.*, 2003; *Binet and Bollinger*, 2005]; however, it suffers from limitations regarding spatial resolution and long-wavelength bias induced by the changing attitude of the satellite. As an example, we show the north-south offsets due to the Landers earthquake measured from a pair of SPOT images with 10 m ground resolution (Figures 2 and 3). This technique is promising for the analysis of future events, especially with the development of higher resolution satellite imagery and an improved control of the satellite attitude (for example using very high resolution SPOT-5 imagery [*Binet and Bollinger*, 2005]). Only a limited number of past earthquakes can be analyzed from this approach due to the lack of available very high resolution satellite images. In the next section we show that air photos can be used in very much the same way, offering better spatial resolution and accuracy near the field than has been achieved with satellite imagery and the possibility to take advantage of existing archives on a number of past large earthquakes.

3. Study Area: The Kickapoo Step Over Along the Landers EQ Fault Trace

[6] In 1992, the M_w 7.3 Landers earthquake ruptured portions of four preexisting faults: the Johnson Valley, the Homestead Valley, Emerson, and Camp Rock faults [e.g., *Sieh et al.*, 1993]. The rupture had a complex geometry with a number of jogs probably due to the nonoptimal orientations of these faults with respect to the preseismic tectonic stress field [*Bouchon et al.*, 1998] (Figure 1). The Kickapoo step over is one of these major jogs (Figure 4). The Johnson Valley Fault (JVF) bends gradually from N15°E to N30°E south of the step over to N30°E north of it. As the fault bends, becoming more and more orthogonal to the maximum direction of horizontal stress [*Hardebeck and Hauksson*, 2001], slip on JVF tapers from nearly 5 m south of the step over to zero over a distance of a few kilometers. North of the step over slip along the Homestead Valley Fault (HVF) is of the order of 3 m. The Landers-Kickapoo fault (LKF), which strikes about N-S and is therefore nearly optimally oriented with respect to the tectonic stress field, is the main zone of deformation connecting JVF and HVF.

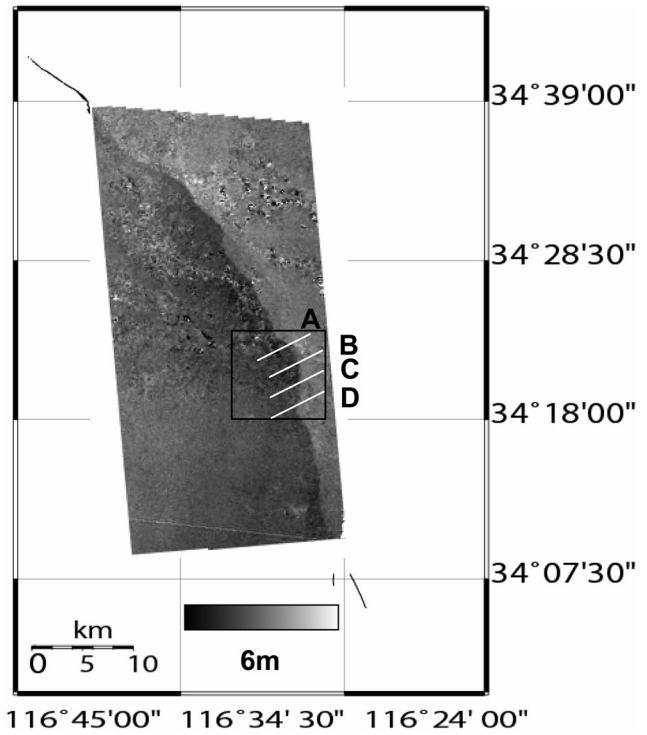

Figure 2. Map of N-S offsets measured from cross correlation of SPOT 4 images of 27 July 1991 and 25 July 1992 [*Van Puymbroeck et al.*, 2000]. Box shows the Kickapoo-Landers area covered by the air photos in Figure 4. The locations of profiles shown in Figure 3 are also indicated.

This zone consists of a 50- to 100-m-wide shear zone with dense fracturing [*Spotila and Sieh*, 1995; *Johnson et al.*, 1994; *Sowers et al.*, 1994]. Interferometric SAR (InSAR) measurements [*Peltzer et al.*, 1994] reveals that the domain west of LKF was tilted southward by an amount consistent with the gradient of vertical slip measured in the field along LKF. The area where LKFF joins HVF has been recognized as a zone of complex and distributed deformation, with dominantly thrust faulting, and has been inferred to correspond to a major slip gap with possible bearing on the rupture dynamics process [*Spotila and Sieh*, 1995]. The joined inversion of SAR and GPS data suggest 1–2 m of shallow slip (at depth less than 5km) and some slip gap at depths between 3 and 10 km [*Fialko*, 2004a, Figure 9]. The joined inversion of seismological and geodetic data indicates that the rupture front was decelerating when rupturing zones of reduced slip, in particular around the Kickapoo step over, and accelerating when rupturing slip asperities [*Hernandez et al.*, 1999].

[7] In Figure 3 we show several profiles in the offset field measured from the SPOT images run across the fault zone in the Kickapoo step over area. These profiles suggest that the total slip across the fault zone is 3.5 ± 0.5 m south of the step over, a value consistent with field measurements, and decreases to about 2.0 ± 0.5 m just north of the step over in the slip gap zone of *Spotila and Sieh* [1995]. So the SPOT offset field suggests the strike-slip offset might in fact not be negligible in this "slip gap zone." The details of the slip

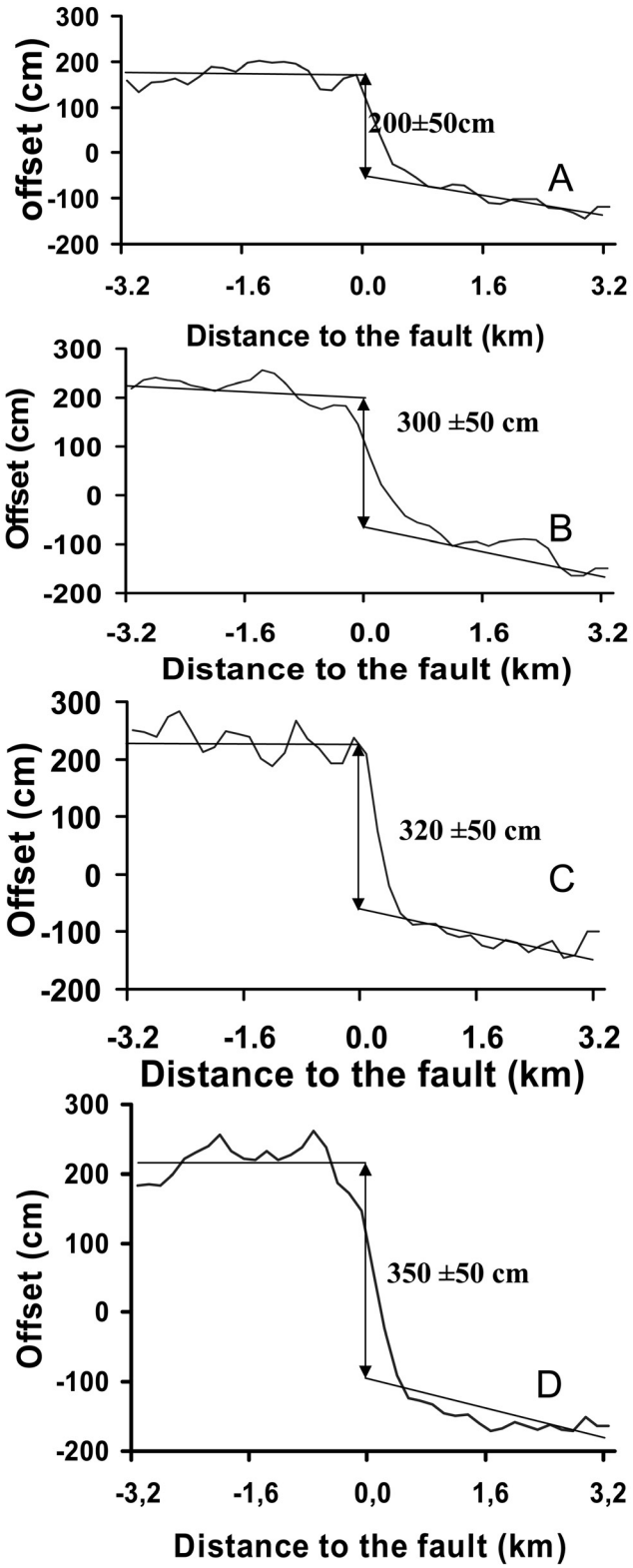

Figure 3. Strike-parallel surface displacement measured from the SPOT images offsets of Figure 2 along profiles A, B, C, and D. See Figure 2 for profiles location. Profile A runs through the slip-gap zone of *Spotila and Sieh* [1995] where field investigations revealed distributed deformation with no measurable offsets. The profile suggests that the total offset across the one might be as large as about 2 m.

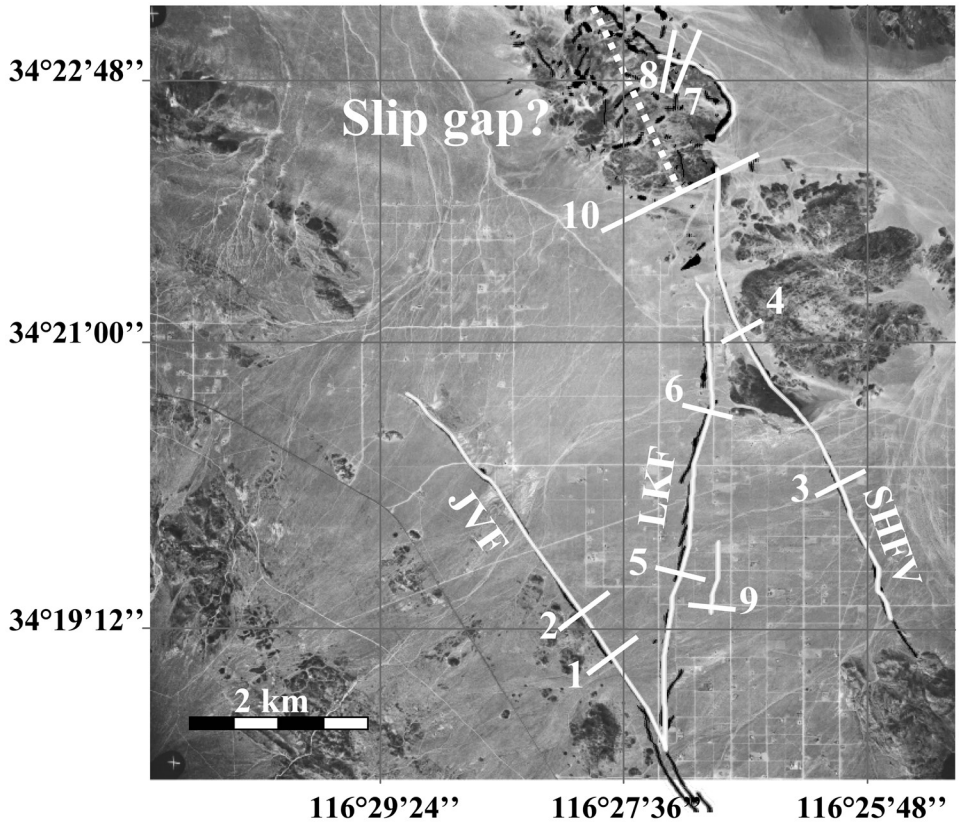

Figure 4. Mapped surface ruptures from *Spotila and Sieh* [1995] (dashed black lines), and ruptures derived from the offset field determined from the air photos (white lines). White segments show location of profiles stacked 200 m along ruptured faults in Figure 9.

distribution and fault rupture are however poorly constrained from these measurements.

4. Data and Method

[8] We have acquired air photos covering the Kickapoo step over and determined surface displacements from subpixel correlation of images acquired before and after the earthquake (Figures 4 and 5). Two images acquired after the Landers earthquakes were used to estimate errors and potential bias associate with this techniques.

4.1. Data

[9] We used film negative from the U.S. National Aerial Photography Program (NAPP) aerial images (Table 1). The images are acquired in a 5–7 years cycle, aircraft altitude is 20,000 feet (6100 m), the focal length is 6 inches (15 cm) and images are 9 by 9 inches (23 by 23 cm) in size covering an area of slightly more than 5 miles (8 km) on a side. Nominal roll, pitch and yaw are zero. Because of the effective geometric and photometric quality of the data the effective ground resolution is about 1 m [*U.S. Geological Survey* (USGS), 1992] while the film nominal resolution is about 10 μm corresponding to 0.4 m on the ground [*Eastman Kodak Company*, 2003]. We used one image acquired on 25 July 1989 before the June 1992 Landers earthquake, and two images acquired after the earthquake (on 10 March 1995 and 1 June 2002). Variations in sun illumination and ground radiometry (including man made and natural evolutions of the scene) yield temporal decorrelation of the images (Figure 5). In order to produce geocoded images we used the 1 arc sec U.S. National Elevation Data Set [*Osborn et al.*, 2001]. Expected vertical accuracy is about 10 m (RMS).

4.2. Processing Flowchart

4.2.1. Digitization

[10] The images were digitized with a microdensitometer nominally designed for astronomical applications (e.g., cartography of stellar objects magnitude) [*Guibert and Moreau*, 1991]. It consists of a 1024 pixels photodiode array with sensitivity centered at 633 nm. Spatial positioning of this instrument mainly relies on a Heidenhain optical ruler with an accuracy of 0.1 μm. Resulting accuracy (i.e., the random error on positioning) and repetitiveness (i.e., the systematic error on positioning) on the scanned images are 0.6 and 0.2 μm, respectively. Images are digitized on 12 bites resulting in a loss the information available from film. However, the resulting quantification noise is typically below the noise induced by temporal decorrelation of the images and thus it does not affect the correlation score and hence the accuracy of measured offset. The very good quality of modulation transfer function (MTF) of the microdensitometer is well suited for this application because it is compatible with the resolution of the film and thus allows correlation of high-frequency features and minimizes the aliasing that has been demonstrated as a source of noise on correlation maps [e.g., *Binet and Bollinger*, 2005].

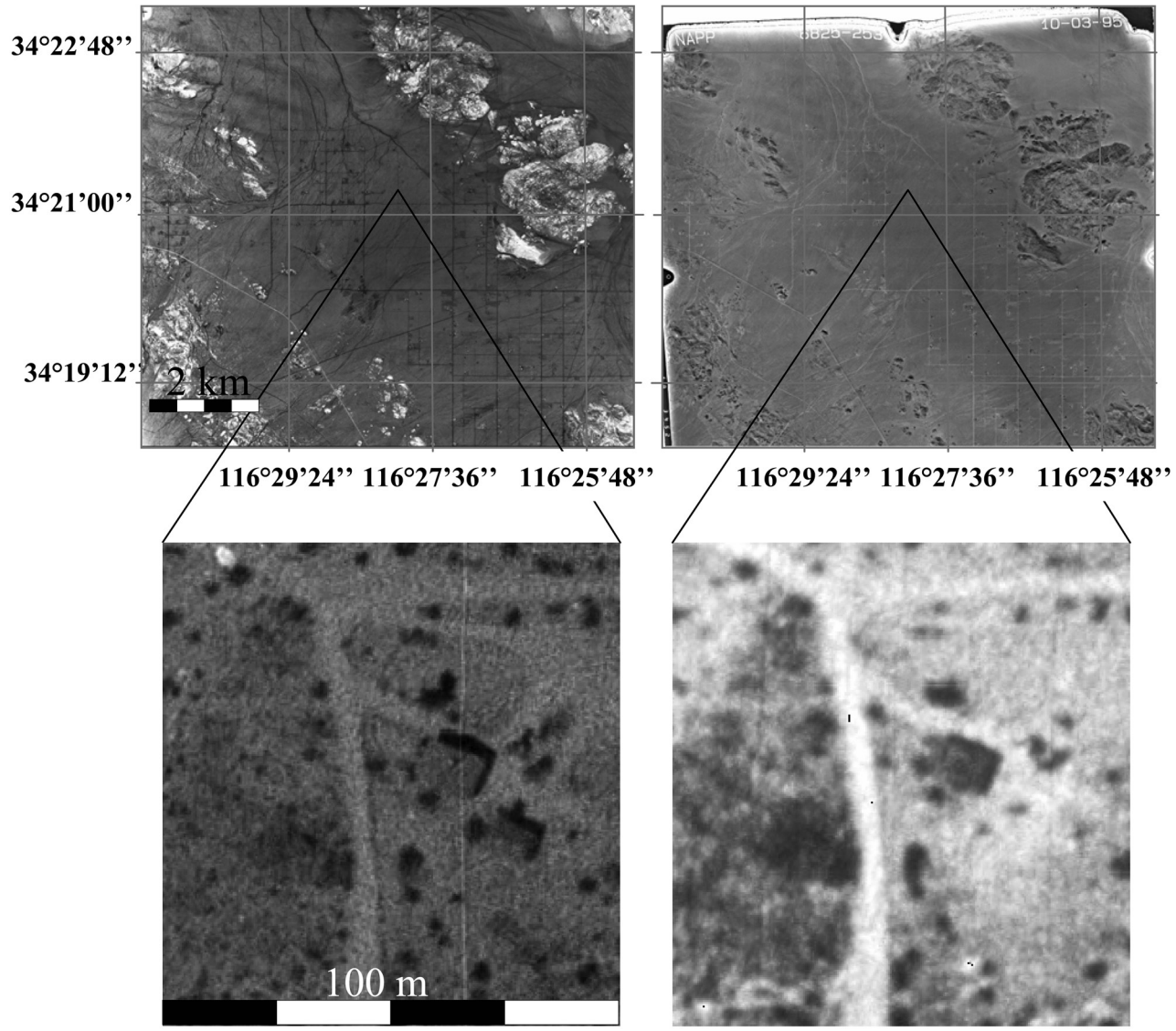

Figure 5. Postearthquake air photos of (left) 25 July 1989 and (right) 10 March 1995 used in this study (bottom) with close-up views at a site with particularly prominent temporal decorrelation. A building visible on left photo is gone in right photo. Temporal decorrelation is the main source of noise on measurement of ground displacement once low spatial artifacts on offset field are filtered out.

4.2.2. Geocoding

[11] Geocoding is the process that assigns a latitude-longitude coordinate to each pixel of the scanned image. It is performed following a three steps procedure. First, a raw geocoded image is generated at the resolution of the DEM (3 arc sec) using the geometrical parameters provided with the images. This image is then correlated with a shaded DEM computed with the appropriate scene illumination, based on the sun position at the time of acquisition of the image. An alternative approach would be to use a reference geocoded image such as a SPOT orthoimage instead of a shaded DEM. The correlation is computed from Symmetrical Phase Only Filter method [*Michel et al.*, 1999a]. This procedure yields a set of ground control points (GCP) with associated uncertainties on the measurement of their coregistration. These GCPs are then used to estimate the parameters of the air photos: roll, pitch, yaw, scene center coordinates, aircraft altitude, and focal length. For the determination of those parameters we use an iterative least squares procedure. Once these parameters are obtained, the image is geocoded in UTM, WGS84 at 0.4 m resolution using a "sinc" resampling kernel 11 × 11 pixels in size [*Van Puymbroeck et al.*, 2000]. Typically several hundred GCP are used and the standard deviation between the GCP positions in the DEM and in the geocoded image, after optimization of the acquisition parameters, is 2.1 m on average.

4.2.3. Subpixel Correlation

[12] We have adapted the correlation technique of *Van Puymbroeck et al.* [2000]. Offsets are computed from the phase shift of the Fourier transform of a sliding window $n \times n$ pixels in size. If the two components of offsets do not exceed $n/4$, it provides a measure of the two horizontal components of the ground displacement with an estimate of

Table 1. Data Set

Material	Source	Reference: Roll-Frame, Date	Characteristics
Images	U.S. National Aerial Photography Program (NAPP)	image 1: 1790-161, 25 Jul 1989; image 2: 6825-253, 10 Mar 1995; image 3: 2498-144, 1 Jun 2002	film negative; 5 miles (8 km) field of view; about 1 m in ground resolution; scene center coordinate 34′20′38″N, 116′28′08″W
Digital elevation model	U.S. National Elevation Dataset (NED)		3 arc sec in planimetric resolution, about 10 m (RMS) in vertical accuracy
Microdensitometer	MAMA (Machine a Mesurer pour l'Astronomie, French national research equipment)	not applicable	12 bites digitations, 10 μm in resolution, 0.6 μm in accuracy, 0.2 μm in repititivity

the uncertainty associated with the quality of the correlation. A linear relationship between correlation score and statistical uncertainty on offset has been derived experimentally. Statistical uncertainty is zero (respectively 0.42) for a correlation score equal to one (respectively 0) With SPOT 10-m resolution images, offsets due to coseismic deformation generally are 1 to 2 pixels because coseismic ground displacements rarely exceed 10 m. On air photos offsets may exceed 10 pixels so the technique developed for SPOT images needed to be adjusted.

[13] We used a multiscale procedure. Experience shows that $n = 32$ is an optimal value to correlate natural scenes. Images are resampled by a decreasing factor equal to 8, 4, 2, and 1. Offsets are computed at each step and values with low correlation score suggesting errors on offsets greater than 0.5 pixels are replaced by local polynomial interpolation. For this procedure a linear relationship between the correlation score and noise on offset has been derived experimentally. For a given resampling factor, the offsets computed at the previous step are used to center the correlation windows in order to measure offsets below the critical $n/4$ value. AA A nearly equivalent approach, using decreasing values of n, yields very similar final results.

[14] The calibration procedure described by *Van Puymbroeck et al.* [2000] is adapted to this procedure. It yields the correction of residual systematic correlation errors that may result from residual aliasing and temporal decorrelation (both sources yield underestimates of the subpixel amplitude of offsets). The calibration function is computed as the difference between theoretical and measured subpixels values. For that purpose, images are artificially shifted by subpixel quantities in the range [0,1] using a "sinc" kernel and white Gaussian noise of various standard deviation are added to simulate different rates of temporal decorrelation [*Van Puymbroeck et al.*, 2000]. The offset fields computed in this study have been obtained with a final 32×32 correlation window and a step of 16 pixels. Note that adjacent measurements are not totally independent since they incorporate information obtained from correlating overlapping multiscale windows. The procedure thus provides independent measurements about every 15 m on the ground.

5. Estimation of Errors and Bias

[15] The procedure was first applied to the two images that were both acquired a couple of years after the Landers earthquake (see Table 2). Resulting postseismic deformation should be negligible so that the actual ground displacement field should be zero (Figure 6). We have measured the apparent offsets between the two images in order to assess the accuracy and potential bias of our procedure. The measured distribution of offsets is centered on zero and is nearly Gaussian with a standard deviation of 0.65 pixels or 26 cm. This yield an empirical estimate of the cumulative effect of all sources of error. This statistical description of errors is somewhat misleading because, as it has also been shown for SPOT images [*Van Puymbroeck et al.*, 2000], the distribution of errors depends strongly on the spatial wavelength. Thus errors cannot be considered a Gaussian white noise (Figure 6b). At wavelengths smaller than 1 km the noise reaches the floor level defined by temporal decorrelation of the images and at larger wavelengths the deformation of films dominates. Figure 6c show the offset map high-pass filtered at wavelength smaller than 1 km. Offset measured below the kilometric scale has noise with a standard deviation as low as 0.18 pixel or 7.2 cm. Wavelengths larger than 1 km were fitted by an order 3 polynomial with maximum-minimum values as large as 2.0 m.

[16] At this step we can conclude that aerial images will provide useful information about earthquake's induced displacements at spatial wavelength smaller than 1 km.

5.1. Optical Distortions

[17] Residual optical distortions due to the camera and thermal image beam deflection near the aircraft result in geometrical distortions of few micrometers on the films [e.g., *Schöler*, 1975]. No calibration is available to com-

Table 2. Error Analysis

	Source of Error	Amplitude	Spatial Frequency
Film	thermomechanical deformation	several pixels	low frequency (see Figure 7d)
Scan	repetitivity and accuracy	below 1/10th of the pixel size	high frequency, line oriented artifact
DEM	uncertainty on elevation and planimetric resolution	typically 10m (RMS) for a 3 arc sec resolution DEM,	correlated to DEM errors
Correlation	scene and SNR-dependent bias	about 1/10th of the pixel size	high frequency (offset map resolution)
Displacements of GCPs	trade-off between viewing parameters and ground deformation	several pixels	low-frequency polynomial

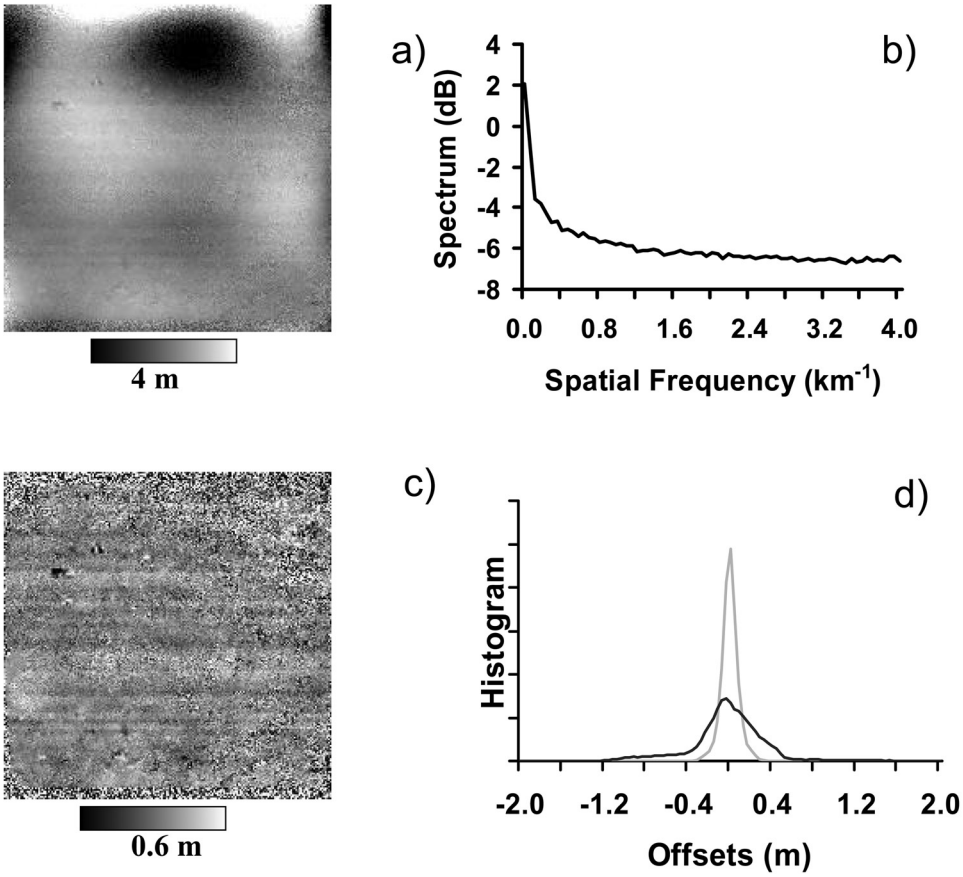

Figure 6. (a) Offset field computed for images with zero ground deformation (images 1 and 2 in Table 1). Correlation window is 32 × 32. It illustrates typical noise on measurement of ground deformation. The low-frequency pattern results from unrecoverable thermomechanical deformation of films and prevents analysis of low-scale deformation of the ground. (b) Spectrum of Figure 6a showing that noise on offset maps is not white and preferentially affects low spatial frequencies. At wavelengths smaller than 1 km the effect the deformation of films is negligible and temporal decorrelation (resulting from changes in radiometry with time) dominates. (c) Figure 6a filtered to remove frequencies below 1 km^{-1}. E-W 100-m-wide stripes result from a scan artifact with amplitude of about 5 cm. Salt and pepper noise results from temporal decorrelation of images. (d) Histograms of Figures 6a (black) and 6c (grey). Filtering reduces dispersion and thus noise on measurements to about the noise level induced by temporal decorrelation. No useful information on ground displacement is available from offset field at wavelength larger than 1 km. Noise at shorter wavelengths is mainly constrained by temporal decorrelation.

pensate for these distortions. They are not automatically compensated during the correlation procedure because they depend on the field and on the optical aperture. Thus they vary within an image because differences in scene centers and flight directions induce varying locations of a given point on the ground on the images. Moreover, these distortions depend on the optical wavelength so they increase by a factor of two on average from blue to red [*Schöler*, 1975], so they cannot be recovered from panchromatic images. This optical distortion results in low-frequency bias on measured offset with a typical magnitude of only a few tenths of centimeters on the ground.

5.2. Film's Deformation

[18] Film suffers temporary and permanent thermomechanical deformations that depend mainly on temperature, relative humidity and age [e.g., *Eastman Kodak Company*, 2003; *Agfa-Gevaert*, 2002]. These deformations are usually isotropic locally but might not be homogeneous. State of the art aerial film is known to suffer temporary deformations of about 20 $\mu m\ m^{-1}\ K^{-1}$ and 20 $\mu m\ m^{-1}$ per percentage of relative humidity. Permanent changes include deformations of about 0.025% resulting from processing and an aging shrinkage of a few hundredths of percent per month for standard storage conditions [*Eastman Kodak Company*, 2003]. The microdensitometer's room is controlled to 20° ± 1°C and about 0.5% relative humidity and the film was scanned a few months after processing. We can thus assume a dimensional stability worse than few tens of microns for our 9 inch (23 cm) films. This term is partly corrected when the viewing parameters are adjusted, so that deformation of the print is modeled as a difference in focal position, viewing angle, and focal length. A large residual error may remain as shown from our test example. No information is available from the published literature about the geometry of the film's deformation. One way to limit

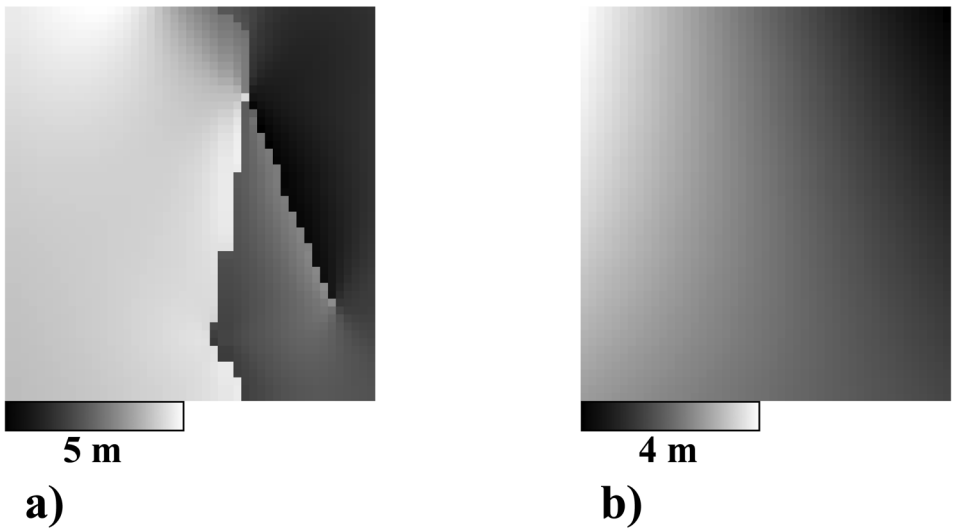

Figure 7. (a) Theoretical coseismic offsets in the study area computed from the model of *Hudnut et al.* [1994]. Because the GCPs lie within the area with significant deformation, their geographic position in the preearthquake and postearthquake images are in fact different. These displacements cannot be measured form the air photos and are compensated when the viewing parameters are optimized during the geocoding procedure. As a result, the model of *Hudnut et al.* [1994] is assumed correct. (b) Long-wavelength component of the offset field removed. To the first order, this offset field is a degree 2 polynomial function because of the near conic projection of aerial images.

this source of noise would be to scan original glass plates. For glass plates, thermomechanical deformations are estimated to be less than about 5 $\mu m\ m^{-1}\ K^{-1}$ and the response to relative humidity is negligible [*Ligterink*, 1971; *USGS*, 1992]. Thus film distortions result in irremediable low-frequency bias with magnitude greater than 1m on the ground and thus put severe limitations on the accuracy of the measured offsets at long wavelength.

5.3. Scanning Errors

[19] The stability of the densitometer is such that scanning errors at the scale of the negative should not exceed 1 μm (see section 4.2 digitization) leading to errors in the offset field of less than about 4 cm on the ground. A line orientated bias pattern with about this amplitude has been detected on the images (Figure 6c). This pattern results from the errors on repetitivity during the line by line scanning procedure. The measured error is 5 times greater than the specified 0.2 μm error in repetitivity (see section 4.2). The wavelength on the ground corresponding to this scanning artifact is about 100m and is compensated on offset maps by assuming line by line invariance of averaged offsets.

5.4. Uncertainty on Viewing Parameters

[20] The geocoding procedure assumes that the images are all tied to a fixed set of GCPs. In the case of SPOT images the GCPs can be chosen in the far field where coseismic displacements are small. This is not the case with the air photos. The offsets of the GCPs due to the earthquake are partly compensated when the viewing parameters of the images are adjusted. These adjustments are generally smaller than the uncertainties on the viewing parameters. The long wavelengths in the offsets field are then mismodeled as resulting from erroneous viewing parameters and are forced to be zero on average for the selected set of GCPs. To illustrate that point, we computed a theoretical model of ground displacement in the study area using the model proposed by *Hudnut et al.* [1994] (Figure 7a). We then estimated the viewing angles that would minimize the quadratic misfit between the observed and predicted position of the GCPs, assumed fixed, for two images that would be acquired before and after the earthquake. Figure 7b shows the long-wavelength offset field that is mismodeled as resulting from differences in viewing angles rather than by ground displacement. This field can be approximated, to within few centimeters, by a degree 2 polynomial function. Indeed, if we neglect relief by assuming a constant elevation within the scene area, the conic projection of aerial images implies that any modification of viewing parameters results in shifting pixels' location according to an order 2 polynomial. During that procedure the displacement field at the GCPS is absorbed by a correction of roll, pitch and yaw by less than 0.02° and a shift of the scene center by only 1m. The corrections are smaller than the nominal uncertainties on these parameters (about 0.1°), therefore there is no hope that the long-wavelength (>5 km) deformation field can be measured from this technique. This is an intrinsic limitation that could be overcome by measuring the GCPs simultaneously with image acquisition, or by assuming values of ground displacements at the GCPs (based for example on some a priori model of coseismic deformation).

5.5. DEM Errors

[21] Because a given point on the ground is not acquired with exactly the same viewing parameters on the two images, vertical uncertainty in the DEM results in scene-dependent geometrical deformation of the geocoded images and consequently contributes to errors in offset. This error is of the order of $\Delta z \times \Delta i$, where Δz and Δi are the vertical error on the DEM and the maximum difference in viewing

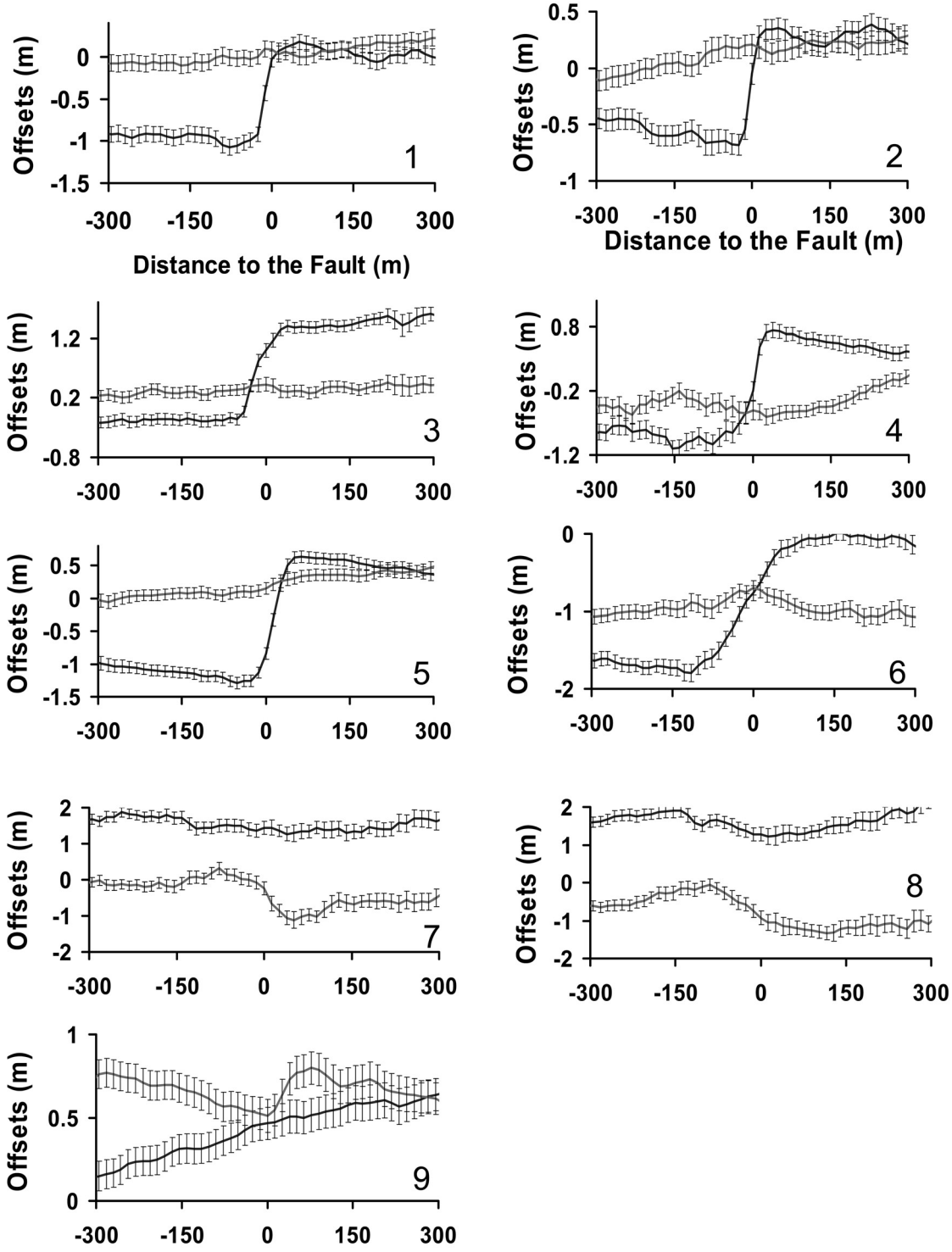

Figure 8. Strike-parallel and strike-perpendicular components of N-S and E-W offsets shown in Figure 10. See Figure 4 for location of profiles. Profiles are stacked 200 m along ruptured faults. All profiles were run perpendicular to the local fault strike. Error bars represents the 3-sigma confidence interval determined from the correlation score. Normal component of displacement is below noise level. Fault rupture zone is typically narrower than 50 m.

angles, respectively. For example, a difference in scene center of 100 m (observed for the images of this study) and a 10 m error in elevation (typical of the 1-sigma uncertainty on elevation in a DEM) result in an apparent, erroneous offset of about 0.2 m between the two geocoded images. Since offsets are measured within an $n \times n$ window, one would expect the error in offset to be divided by square root of $2xn$. Unfortunately, because of systematic errors

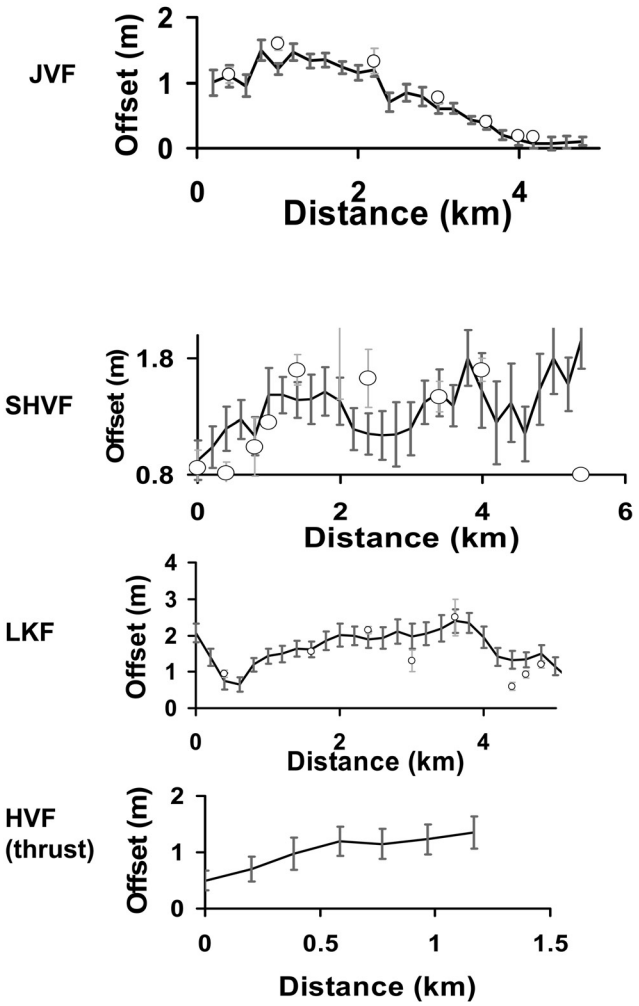

Figure 9. Slip distribution along JVF, SHVF, LKF, and HVF derived from stacked profiles across the air photo offsets field. Independent measurements are every 200 m. The offsets measured from the air photos are generally consistent with field measurements (open circles), except at some places (e.g., along northern SHVF segment) where no visible surface offsets could be measured in the field.

resulting in part from the poorer spatial resolution of the DEM, the error reduction is not that much ($\sim$1 cm for n = 32). Errors in measurements of offset due to the DEM errors will be correlated with the DEM and will be typically be smaller than a few centimeters in the present study for a correlation window of 32 $\times$ 32 in size. The use of a SRTM DEM would yield about the same accuracy.

5.6. Decorrelation

[22] Images of natural scenes acquired at different dates suffer temporal decorrelation resulting mainly from changes in surface radiometry, in atmospheric and illumination conditions and in viewing and detection parameters.

[23] Most rates of temporal decorrelation increase with the spatial frequency because landscape generally varies more rapidly at high spatial frequencies than at low frequencies. We can thus foresee a greater rate of temporal decorrelation per pixel for images with meter or submeter resolution than for SPOT decametric imagery. The contribution of the temporal decorrelation to the uncertainty in the measured offsets can be estimated from the local correlation score [*Van Puymbroeck et al.*, 2000]. This score does not provide information about the prominent low-frequency (spatial frequency lower than $1/n$ pixel^{-1}, where n is the size of the correlation window) sources of noise and bias on offsets listed above.

[24] In this study the correlation score is used as a weighting factor during the stacking procedure of profiles on offset across the ruptured fault zone (Figures 8 and 9). Averaged correlation score is 0.61 corresponding to decorrelation in offset equal to 0.23 pixel on average or about 10 cm on the ground.

6. Measurement of Coseismic Deformation in the Kickapoo Step Over Area

[25] Results obtained from applying the procedure described below to the images of the Kickapoo step over acquired before and after the Landers earthquake are shown in Figure 10. Discontinuities in the measured N-S and E-W offset field clearly show up and correlate with the fault ruptures mapped in the field [*Spotila and Sieh*, 1995] (Figure 4). At high frequency (for wavelengths less than about 1 km) the noise level estimated from the correlation score is about 21 cm at the 3-sigma confidence level. Distortions at longer wavelength are up to 4 m in amplitude. These distortions do not affect the determination of the fault geometry nor the possibility of measuring the fault slip across the fault zone.

[26] The horizontal component of fault slip was determined from profiles run perpendicular to the fault trace. In Figure 8 such profiles are stacked 200 m along fault segments. Because of the slightly sinuous fault geometry the stacked profiles might be taken to suggest a shear zone with finite width. Close inspection of the offset field reveals that the high strain zone corresponding to the fault ruptures is very narrow, typically less than 50 m, except in the seismic gap zone (located in Figure 4). It might be even less but a narrower width cannot be resolved with the correlation window (32 $\times$ 32). These profiles clearly indicate that these faults are purely strike slip except for the Homestead Valley fault segment north of junction with the Landers-Kickapoo fault, which is a pure thrust fault (profiles 7 and 8 in Figure 8). The amount of fault slip was measured by fitting 0.6-km-long profiles across the fault as the sum of a step function and a linear term. These measurements were made every 200 m by stacking the profiles within each 200-m-wide swath (Figure 9). The uncertainty on fault slip (defined as the amplitude of the step function) was estimated from the RMS of the fit to each profile. Our measurements agree remarkably well with the field measurements of *Spotila and Sieh* [1995] along the JVF, the LKF, and the southern segment of the Homestead Valley fault (SHVF). The greatest discrepancy is along the northern end of the LKF where the ground rupture becomes more complicated near the junction with Homestead Valley Fault.

[27] Although the fractures were identified and mapped in the field, no measurements of the fault slip could be done in the field along the secondary fault zone which parallels LKF

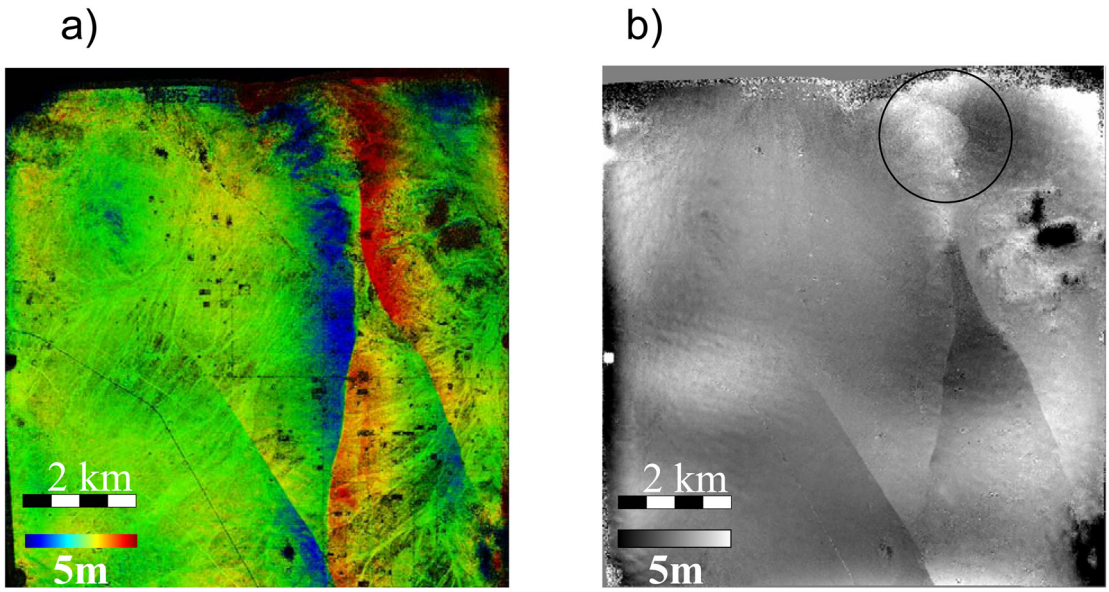

Figure 10. Composite image showing the N-S offset map (hue) and (a) the correlation score (intensity) and (b) E-W offsets. Ruptured fault trace and ground displacements appear smoother and more regular at this scale than from field investigation. N-S offsets north of rupture indicates smooth deformation rather than reported slip gap by *Spotila and Sieh* [1995], suggesting that complexity of rupture is limited to local superficial asperity (Figure 4). E-W offset induced by reported thrust fault north of the rupture is clearly visible [*Spotila and Sieh*, 1995] (black circle). Note artifact at wavelengths larger than 1 km resulting from unrecoverable thermomechanical deformation of films. This artifact does not interfere with estimate of surface slip but prevents analysis of slip distribution at depth. Spatial resolution is 12.8 m, independent measurement every about 15 m.

corresponding to profile 9 in Figures 4 and 8. Profile reveals an average of 20 ± 7 cm of strike-slip displacement across that feature. This example shows that relatively subtle features, not easily measurable in the field, can be identified and measured from air photos offsets.

[28] Figure 11 shows a stack of all profiles within a 2-km-wide swath across the surface slip gap zone (see location in Figure 4). This profile suggests that there is no localized rupture, but a relatively diffuse shear zone about 1 km wide. It is unfortunately located in an area of large low spatial frequency artifact (Figure 10) so that elastic modeling of slip at depth cannot be carried out. This shear zone corresponds closely with distributed ground ruptures observed in the field [*Spotila and Sieh*, 1995] (Figure 4). The displacement across each of these individual fractures, which are too small to show up in the air photos offsets, could not be measured in the field. The air photo offsets

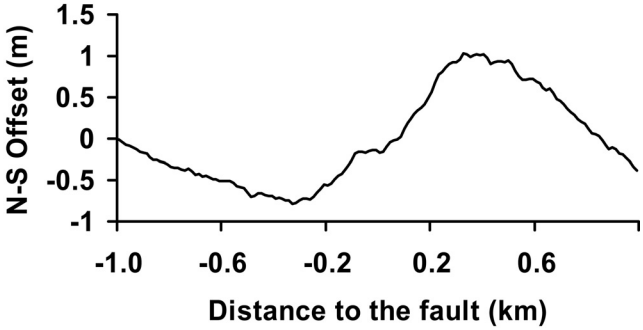

Figure 11. Profile across the slip gap zone (profile 10 in Figure 4). Only the strike-parallel component of slip (for a fault represented by dashed line on Figure 4) is shown. Deformation is not localized but distributed across a 2-km-wide shear zone. The total offset across the shear zone is difficult to estimate with confidence due to possible trade-off with deformation of the films at this scale. Our estimate ranges between 1.7 and 3 m.

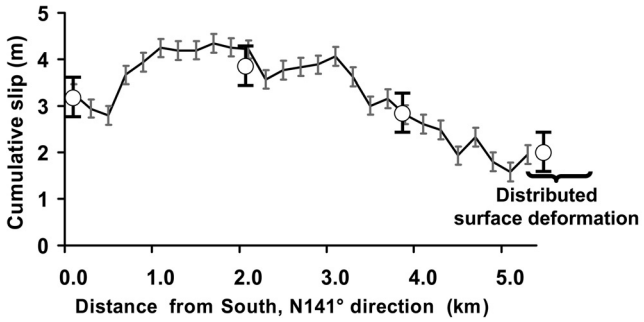

Figure 12. Cumulative slip distribution across the fault zone (3-sigma error bars). White circles represent slip measured from SPOT and associated uncertainty (Figure 3). Measurements from SPOT and air photos are in good agreement and do not suggest any slip gap area as reported from field investigation [*Sieh et al.*, 1993].

show that the total slip across the shear zone is between 2 and 3 m. This measurement is consistent with the ~2.0 m slip measured from the SPOT offsets (Figure 3) and is slightly greater than the 1–2 m shallow slip patch inferred from SAR images [*Fialko*, 2004a]. (Figure 12).

7. Some Seismotectonic Implications

7.1. Fault Geometry, Localized Fault Slip Versus Distributed Anelastic Shear

[29] The offset field reveals the geometry of the faults which ruptured during the Landers earthquake. The Landers-Kickapoo fault shows a sinuosity at the kilometric scale (Figure 10). Geomorphic discontinuity observed on the pre-Landers earthquake image suggest that the Landers-Kickapoo fault existed before that earthquake, but it is clearly a young feature and the observed sinuosity might be reminiscent of en echelon Riedel shears which first formed across the step over [*Ahlgren*, 2001]. By contrast the Johnson Valley fault is much more linear, as expected for a fault with more cumulative slip [*Wesnousky*, 1988].

[30] The consistency between the measurements of fault slip measured in the field and from the air photos offset show that surface slip measured more than 2 years after the earthquake matches those measured in the field immediately after the event. We therefore do not see any resolvable afterslip from our technique. This is consistent with studies of postseismic deformation which found evidence for essentially deep afterslip or viscoelastic relaxation or poroelastic rebound [*Fialko*, 2004b; *Peltzer et al.*, 1998; *Savage et al.*, 2003]. It also shows that once a localized fault is formed very little deformation is absorbed off the main fault trace. However, field measurements might be affected by some variability below the scale captured by the air photos offsets. In that case the field measurements might significantly underestimate the total slip but we believe, based in this example that this generally does not occur when a major fault trace clearly dominates the fault pattern. This means that field measurements of slip (associated either with a recent or a paleoseismic events) along a well-expressed major fault trace are probably generally representative of the total slip across the fault zone. The fact that we reach this conclusion in a zone where the fault geometry is relatively complex implies that strain localization on a single fault probably does not require much cumulative slip. Given that the cumulative slip on JVF and SHVF is estimated to only about 300 m and that cumulative slip on LKF must be significantly less [*Spotila and Sieh*, 1995], a cumulative displacement of the order of 100 m might be sufficient for strain to localize on a major fault.

[31] Our measurements confirm that the portion of Homestead Valley fault north of the intersection with LKF was a zone of relatively lower fault slip during the Landers event, as proposed by *Sieh et al.* [1993] and *Spotila and Sieh* [1995]. The fact that no well-localized fault zone was able to form there is probably due to the fact that the intersection between the LKV and the SHV strike-slip faults is not stable. Cumulative deformation has induced bending of the Homestead Valley fault and distributed deformation in the area surrounding the faults junction. In this case, although cumulative slip is large, the instability of the junction has prevented the formation of a localized fault zone.

[32] We conclude that once stable fault zone geometry is attained the development of well-localized fault zone probably requires less than a few hundred meters cumulative slip.

7.2. Implication for the Determination of the Critical Strain Before Anelastic Failure

[33] Surface strain produced by the Landers earthquake yield information on the critical strain which can be sustained elastically by near surface rocks. The discussion below relies on the following rationale. (1) Any distributed strain with a sense of shear opposite to that on nearby fault ruptures has to be elastic since it can only reflect elastic rebound. (2) Any distributed strain with the same sense of shear as on the nearby fault could be elastic or anelastic. If fractures were observed in the field, it suggests that anelastic yielding was reached. Otherwise, it is impossible to discard the possibility of distributed anelastic deformation with fractures too small to be recognized and mapped in the field.

[34] Lateral variation of slip along the JV, SHV, and LK faults implies coseismic fault-parallel elongation or contraction of the surrounding medium of the order of 0.5×10^{-3} (typically 0.5 m 1 km^{-1}) (Figure 9). The best constraints come from the gradual northward tapering of slip along the JVF. This deformation must be primarily elastic since field investigations did not reveal any evidence for fracturing that would have resulted from this strain [*Spotila and Sieh*, 1995; *Sowers et al.*, 1994]. Profiles run perpendicular to the fault also indicate typical value of shear strain of the same order of magnitude with a sense of shear opposite to that on the fault (Figure 11). We conclude that that the near surface rocks in the Landers area could sustain strain as large as 0.5×10^{-3} without visible fracturing, placing a lower bound on the limit for anelastic yielding.

[35] Surface strain in the "surface slip gap" area provides an idea of an upper bound. Our measurements indicate that the fault parallel displacement is of the order of 2 m (Figure 11). This deformation is not localized on a single fault but rather distributed within a 1-km-wide shear zone, within which the strain is about 2×10^{-3}. Fractures were observed in the field within this shear zone [*Spotila and Sieh*, 1995] (Figures 1 and 4). We infer that this strain exceeds the maximum elastic strain sustainable by near surface rocks. This estimate might be compared with results from rock mechanics experiments. Experiments carried on initially intact westerly granite show that, at confining pressure of less than about 50MPa (corresponding to depths shallower than 2 km), the critical strain for fault strain localization, at the scale of laboratory samples, would be of the order of $1–2 \times 10^{-3}$ [*Lockner*, 1998]. We therefore conclude that, during coseismic deformation, the critical strain for anelastic yielding of surface rocks in the Landers area is of the order of 1×10^{-3}, and that anelastic strain in excess of about $1–2 \times 10^{-3}$ is necessary for strain localization and hence strain drop. We speculate that the propagation of the rupture front across the slip gap area was a sink of energy. This is because distributed faulting absorbs more energy than slip on a single fault plane. This might have impeded the rupture propagation as suggested by the

decrease in rupture velocity [*Wald and Heaton*, 1994; *Hernandez et al.*, 1999].

8. Conclusion

[36] Near-field coseismic ground deformation can be measured from air photos using a correlation technique analogous to that developed for satellite imagery [*Michel et al.*, 1999a; *Van Puymbroeck et al.*, 2000]. This approach is a useful complement to other remote sensing techniques, such as SAR interferometry, or field investigations. Limitations of the technique are essentially due to possible deformation of the films and incomplete knowledge of the image parameters (position, elevation of the plane). The development of new survey techniques for digital air photos acquisition in which the plane position is determined from real time kinematics GPS will help overcome these problems. In spite of these limitations the technique can be used to map fault ruptures to within a few tens of meters and measure fault slip with a resolution of about 10–20 cm with a sampling rate of a few points per kilometers.

[37] **Acknowledgments.** This paper has benefited greatly from reviews by two anonymous reviewers and the AE Sandy Steacy. This study was supported by the Action Concertée Incitative "Catastrophes Naturelles" of INSU. We thank NSF for partial support through grant EAR-0409652. This is Tectonics Observatory contribution 14.

References

Agfa-Gevaert (2002), Panchromatic negative film for aerial photography, aviphot pan 400s PE 1, Mortsel, Belgium, Oct.

Ahlgren, S. G. (2001), The nucleation and evolution of Riedel shear zones as deformation bands in porous sandstones, *J. Struct. Geol.*, *23*(8), 1203–1214.

Binet, R., and L. Bollinger (2005), Horizontal coseismic deformation of the 2 003 Bam (Iran) earthquake measured from SPOT-5 THR satellite imagery, *Geophys. Res. Lett.*, *32*, L02307, doi:10.1029/2004GL021897.

Bouchon, M., M. Campillo, and F. Cotton (1998), Stress field associated with the rupture of the 1992 Landers, California, earthquake and its implications concerning the fault strength at the onset of the earthquake, *J. Geophys. Res.*, *103*, 21,091–21,097.

Crippen, R. E. (1992), Measurement of subresolution terrain displacements using SPOT panchromatic imagery, *Episodes*, *15*, 56–61.

Dominguez, S., J. Avouac, and R. Michel (2003), Horizontal coseismic deformation of the 1999 Chi-Chi earthquake measured from SPOT satellite images: Implications for the seismic cycle along the western foothills of central Taiwan, *J. Geophys. Res.*, *108*(B2), 2083, doi:10.1029/2001JB000951.

Eastman Kodak Company (2003), Aerochrome HS film SO-359, *Publ. AS-207*, Rochester, N. Y.

Fialko, Y. (2004a), Probing the mechanical properties of seismically active crust with space geodesy: Study of the coseismic deformation due to the 1992 M_w 7.3 Landers (southern California) earthquake, *J. Geophys. Res.*, *109*, B03307, doi:10.1029/2003JB002756.

Fialko, Y. (2004b), Evidence of fluid-filled upper crust from observations of postseismic deformation due to the 1992 M_w7.3 Landers earthquake, *J. Geophys. Res.*, *109*, B08401, doi:10.1029/2004JB002985.

Guibert, J., and O. Moreau (1991), Photographic astronomy with MAMA, *Messenger*, *64*, 69–70.

Hardebeck, J. L., and E. Hauksson (2001), Crustal stress field in southern California and its implications for fault mechanics, *J. Geophys. Res.*, *106*, 21,859–21,882.

Hernandez, B., F. Cotton, and M. Campillo (1999), Contribution of radar interferometry to a two-step inversion of the kinematics process of the 1992 Landers earthquake, *J. Geophys. Res.*, *104*, 13,083–13,099.

Hudnut, K. W., et al. (1994), Coseismic displacements of the 1992 Landers earthquake sequence, *Bull. Seismol. Soc. Am.*, *84*, 625–645.

Johnson, M., A. Linde, and D. Agnew (1994), Continuous borehole strain in the San Andreas fault zone before, during and after the 28 June 1992, M_w = 7.3 Landers, Calif. earthquake, *Bull. Seismol. Soc. Am.*, *84*, 799–805.

Ligterink, G. H. (1971), Film-glass differences, in *International Symposium on Image Deformation*, pp. 269–273, FREG, Ottawa, Ont., Canada.

Lockner, D. A. (1998), A generalized law for brittle deformation of Westerly granite, *J. Geophys. Res.*, *103*, 5107–5123.

Massonnet, D., M. Rossi, C. Carmona, F. Adragna, G. Peltzer, K. Feigl, and T. Rabaute (1993), The displacement field of the Landers earthquake mapped by radar interferometry, *Nature*, *364*, 138–142.

McGill, S. F., and C. M. Rubin (1999), Superficial slip distribution on the central Emerson fault during the June 28, 1992, Landers earthquake, California, *J. Geophys. Res.*, *104*, 4811–4833.

Michel, R., J. P. Avouac, and J. Taboury (1999a), Measuring ground displacements from SAR amplitude images: Application to the Landers earthquake, *Geophys. Res. Lett.*, *26*, 875–878.

Michel, R., J. P. Avouac, and J. Taboury (1999b), Measuring near field coseismic displacements from SAR images: Application to the Landers earthquake, *Geophys. Res. Lett.*, *26*, 3017–3020.

Osborn, K., J. List, D. Gesch, J. Crowe, G. Merrill, E. Constance, J. Mauck, C. Lund, V. Caruso, and J. Kosovich (2001), National digital elevation program (NDEP), in *Digital Elevation Model Technologies and Applications: The DEM Users Manual*, edited by D. Maune, pp. 83–120, Am. Soc. for Photogramm. and Remote Sens., Bethesda, Md.

Peltzer, G., K. W. Hudnut, and K. L. Feigl (1994), Analysis of coseismic surface displacement gradients using radar interferometry: New insights into the Landers earthquake, *J. Geophys. Res.*, *99*, 21,971–21,981.

Peltzer, G., P. Rosen, F. Rogez, and K. Hudnut (1998), Poroelastic rebound along the Landers 1992 earthquake surface rupture, *J. Geophys. Res.*, *103*, 30,131–30,145.

Peltzer, G., F. Crampé, and G. King (1999), Evidence of non-linear elasticity of the crust from the M_w7.6 Manyi (Tibet) earthquake, *Science*, *286*, 272–276.

Savage, J. C., J. L. Svarc, and W. H. Prescott (2003), Near-field postseismic deformation associated with the 1992 Landers and 1999 Hector Mine, California, earthquakes, *J. Geophys. Res.*, *108*(B9), 2432, doi:10.1029/2002JB002330.

Schöler, H. (1975), On photogrammetric distortion, *Photogramm. Eng. Remote Sens.*, *41*(6), 761–769.

Sieh, K., et al. (1993), Near-field investigations of the Landers earthquake sequence, April to July 1992, *Science*, *260*, 171–176.

Simons, M., Y. Fialko, and L. Rivera (2002), Coseismic deformation from the 1999 M_w 7.1 Hector Mine, California, earthquake as inferred from InSAR and GPS observations, *Bull. Seismol. Soc. Am.*, *92*, 1390–1402.

Sowers, J. M., J. R. Unruh, W. R. Lettis, and T. D. Rubin (1994), Relationship of the Kickapoo fault to the Johnson Valley and Homestead Valley faults, San Bernardino County, California, *Bull. Seismol. Soc. Am.*, *84*, 528–536.

Spotila, J. A., and K. Sieh (1995), Geologic investigation of a "slip gap" in the superficial ruptures of the 1992 Landers earthquake, southern California, *J. Geophys. Res.*, *100*, 543–559.

U.S. Geological Survey (1992), The National Aerial Photography Program (NAPP), fact sheet, 1 p., Reston, Va.

Van Puymbroeck, N., R. Michel, R. Binet, J. P. Avouac, and J. Taboury (2000), Measuring earthquakes from optical satellite images, *Appl. Opt. Inf. Process.*, *39*(23), 3486–3494.

Wald, D., and T. Heaton (1994), Spatial and temporal distribution of slip for the 1992 Landers, California, earthquake, *Bull. Seismol. Soc. Am.*, *84*, 668–691.

Weldon, R. J., J. P. McCalpin, and T. K. Rockwell (1996), Paleoseismology of strike-slip tectonic environments, in *Techniques in Paleoseismology*, pp. 271–329, Elsevier, New York.

Wesnousky, S. G. (1988), Seismological and structural evolution of strike-slip faults, *Nature*, *335*, 340–342.

Yeats, R. S., K. E. Sieh, and C. R. Allen (1997), *The Geology of Earthquakes*, Oxford. Univ. Press, New York.

J.-P. Avouac, Tectonics Observatory, Geological and Planetary Sciences, California Institute of Technology, Mail Code 100-23, Pasadena, CA 91125, USA. (avouac@gps.caltech.edu)

R. Michel, Laboratoire de Détection et de Géophysique, CEA, BP 12, F-91680 Bruyères-le-Châtel Cedex, France. (remi.michel@cea.fr)